



» Chemosensors

Chemosensors

Q1

Q2

Q3

Q4

Powered by WoS-Journal.Info

» JIF 2023:3.7

</> Get Embedded Code

Save the journal to Dashboard

ABBREVIATION: CHEMOSENSORS

ISSN: N/A

EISSN: 2227-9040

CATEGORY: INSTRUMENTS & INSTRUMENTATION - SCIE
CHEMISTRY, ANALYTICAL - SCIE
ELECTROCHEMISTRY - SCIE

WoS CORE CITATION INDEXES: SCIE - Science Citation Index Expanded

JOURNAL IMPACT FACTOR (JIF): 3.7

5-YEAR IMPACT FACTOR: 3.7

BEST RANKING: INSTRUMENTS & INSTRUMENTATION (Q1) — Percentage rank: 77.6%

OPEN ACCESS SUPPORT: Fully Open Access — It may take a publication fee. For more info, check it on DOAJ.ORG

COUNTRY: SWITZERLAND

STATUS IN WoS CORE: ACTIVE ●

PUBLISHER: MDPI AG

Share





Submit to *Chemosensors*

Review for *Chemosensors*

Share

Journal Menu

- Chemosensors Home
- Aims & Scope
- Editorial Board
- Reviewer Board
- Topical Advisory Panel
- Photography Exhibition
- Instructions for Authors
- Special Issues
- Topics
- Sections & Collections
- Article Processing Charge
- Indexing & Archiving
- Editor’s Choice Articles
- Most Cited & Viewed
- Journal Statistics
- Journal History
- Journal Awards
- Conferences
- Editorial Office

Journal Browser

volume

▼

issue

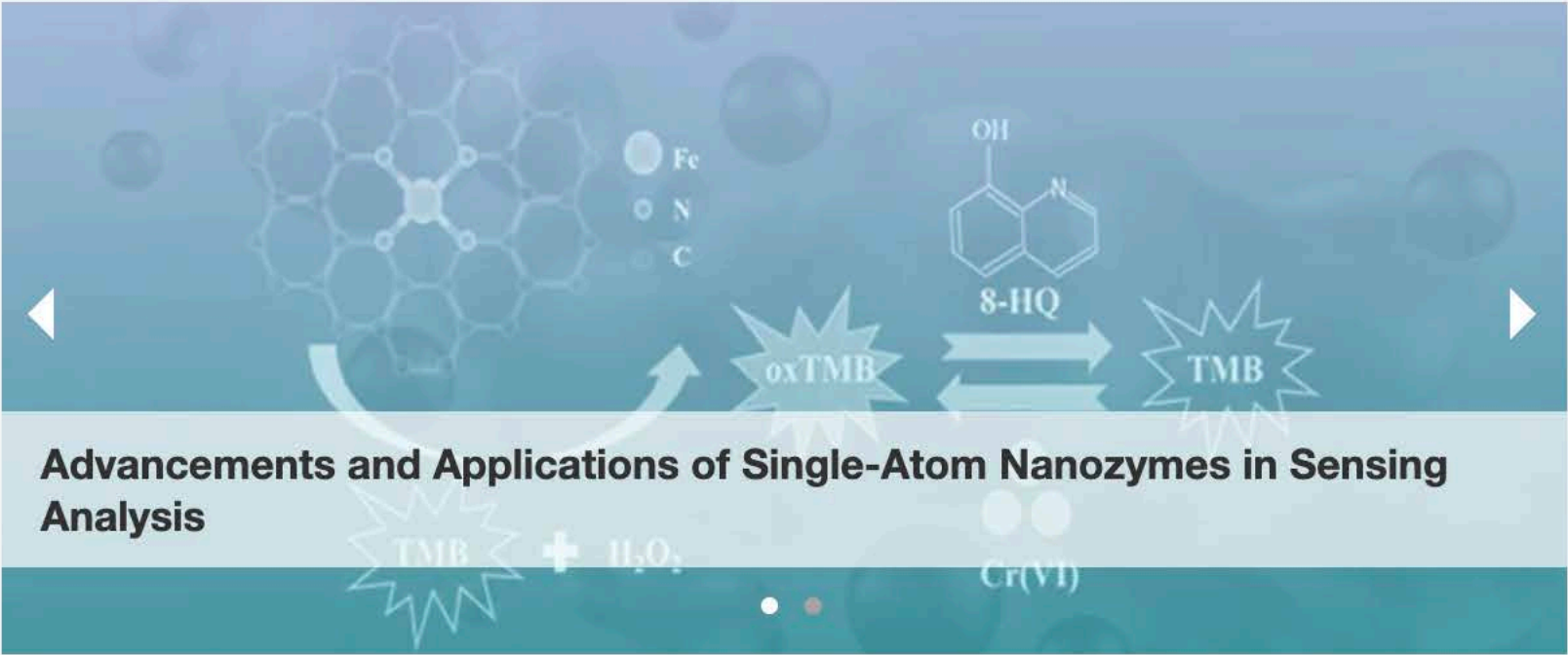
▼

Go

- > Forthcoming issue
- > Current issue

Vol. 12 (2024)	Vol. 6 (2018)
Vol. 11 (2023)	Vol. 5 (2017)
Vol. 10 (2022)	Vol. 4 (2016)
Vol. 9 (2021)	Vol. 3 (2015)
Vol. 8 (2020)	Vol. 2 (2014)
Vol. 7 (2019)	Vol. 1 (2013)

Highly Accessed Articles



Chemosensors

Chemosensors is an international, scientific, **peer-reviewed**, open access journal on the science and technology of chemical sensors and related analytical methods and systems, published monthly online by MDPI.

- Open Access** — free for readers, with **article processing charges (APC)** paid by authors or their institutions.
- High Visibility:** indexed within **Scopus, SCIE (Web of Science), CAPlus / SciFinder, Inspec, Engineering Village** and **other databases**.
- Journal Rank:** JCR - Q1 (Instruments and Instrumentation) / CiteScore - Q2 (*Analytical Chemistry*)
- Rapid Publication:** manuscripts are peer-reviewed and a first decision is provided to authors approximately 17.1 days after submission; acceptance to publication is undertaken in 2.6 days (median values for papers published in this journal in the first half of 2024).
- Recognition of Reviewers:** reviewers who provide timely, thorough peer-review reports receive vouchers entitling them to a discount on the APC of their next publication in any MDPI journal, in appreciation of the work done.

Impact Factor: 3.7 (2023); 5-Year Impact Factor: 3.7 (2023)

Imprint Information Journal Flyer Open Access ISSN: 2227-9040

Latest Articles

Open Access

Article

11 pages, 1227 KiB

Sampling and Comparison of Extraction Techniques Coupled with Gas Chromatography–Mass Spectrometry (GC-MS) for the Analysis of Substrates Exposed to Explosives

by Himanshi Upadhyaya, Alexis J. Hecker and John V. Goodpaster

Chemosensors **2024**, 12(12), 251; <https://doi.org/10.3390/chemosensors12120251> - 29 Nov 2024

Abstract Explosive-detecting canines (EDCs) show high sensitivity in detecting explosives that they are trained to detect. The ability of canines to detect explosive residues to the parts per trillion level can sometimes result in nuisance alerts. These nuisance alerts can occur when various materials [...] **Read more.**

(This article belongs to the Special Issue **Detection of Volatile Organic Compounds in Complex Mixtures**)

Show Figures

IMPACT FACTOR 3.7

CITESCORE 5.0

E-Mail Alert

Add your e-mail address to receive forthcoming issues of this journal:

Enter Your E-Mail Address...

Subscribe

News

22 November 2024
Chemosensors | Top 10 Highly Cited Reviews in 2023

13 November 2024
Meet Us at the 38th IEEE International Conference on Micro Electro Mechanical Systems (IEEE MEMS 2025), 19–23 January 2025, Kaohsiung, Taiwan



5 November 2024
MDPI INSIGHTS: The CEO's Letter #17 - OA Week, Basel Open Day, Beijing Graphene Forum

More News & Announcements...

Topics



Propose a Topic

Topic in *Analytica, Foods, Molecules, Separations, Chemosensors, Processes*
Application of Liquid Chromatography-Mass Spectrometry and Related Techniques
Topic Editors: Chao Kang, Ronald Beckett
Deadline: 15 December 2024

Topic in *Beverages, Foods, Molecules, Nutrients, Separations, Chemosensors*
Advances in Analysis of Food and Beverages
Topic Editors: Anna M. Kaczmarek, Constantinos G. Triantafyllidis

Article

The Influence of Temperature on the Spatial Distribution of AuNPs on a Ceramic Substrate for Biosensing Applications

Yazmín Mariela Hernández-Rodríguez ¹, Esperanza Baños-López ², Pablo Damián-Matsumura ³,
Claudia Haydée González de la Rosa ^{4,*}  and Oscar Eduardo Cigarroa-Mayorga ^{1,*} 

¹ Advanced Technologies Department, UPIITA-Instituto Politécnico Nacional, Av. IPN 2580, Col. Ticomán, Mexico City 07340, Mexico; yazmin.hernandez@cinvestav.mx

² Academia de Química, Universidad Autónoma del Estado de Hidalgo (UAEH), Carretera Pachuca-Tulancingo Km. 4.5., Pachuca 42184, Mexico; esperanza_banos10303@uah.edu.mx

³ Department of Biology of Reproduction, Biological Sciences and Health Division (DCBS), Autonomous Metropolitan University (UAM), Mexico City 09310, Mexico; pdamian@izt.uam.mx

⁴ Departamento de Ciencias Naturales, Unidad Cuajimalpa, Universidad Autónoma Metropolitana, Mexico City 05348, Mexico

* Correspondence: cgonzalez@cua.uam.mx (C.H.G.d.l.R.); ocigarroam@ipn.mx (O.E.C.-M.)

Abstract: In this study, we investigated the spatial distribution and homogeneity of gold nanoparticles (AuNPs) on an alumina (Al₂O₃; AAO) substrate for potential application as surface-enhanced Raman scattering (SERS) sensors. The AuNPs were synthesized through thermal treatment at 450 °C at varying times (5, 15, 30, and 60 min), and their distribution was characterized using field-emission scanning electron microscopy (FE-SEM) and scanning transmission electron microscopy (STEM). The FE-SEM and STEM analyses revealed that the size and interparticle distance of the AuNPs were significantly influenced by the duration of thermal treatment, with shorter times promoting smaller and more closely spaced nanoparticles, and longer times resulting in larger and more dispersed particles. Raman spectroscopy, using Rhodamine 6G (R6G) as a probe molecule, was employed to evaluate the SERS enhancement provided by the AuNPs on the AAO substrate. Raman mapping (5 μm × 5 μm) was conducted on five sections of each sample, demonstrating improved homogeneity in the SERS effect across the substrate. The topological features of the AuNPs before and after R6G incubation were analyzed using atomic force microscopy (AFM), confirming the correlation between a decrease in surface roughness and an increase in R6G adsorption. The reproducibility of the SERS effect was quantified using the maximum intensity deviation (D), which was found to be below 20% for all samples, indicating good reproducibility. Among the tested conditions, the sample synthesized for 15 min exhibited the most favorable characteristics, with the smallest average nanoparticle size and interparticle distance, as well as the most consistent SERS enhancement. These findings suggest that AuNPs on AAO substrates, particularly those synthesized under the optimized condition of 15 min at 450 °C, are promising candidates for use in SERS-based sensors for detecting cancer biomarkers. This could be attributed to temperature propagation promoted at the time of synthesis. The results also provide insights into the influence of thermal treatment on the spatial distribution of AuNPs and their subsequent impact on SERS performance.

Keywords: gold nanoparticles (AuNPs); aluminum oxide; two-step anodization; SERS substrates; thermal treatment



Citation: Hernández-Rodríguez, Y.M.; Baños-López, E.; Damián-Matsumura, P.; González de la Rosa, C.H.; Cigarroa-Mayorga, O.E. The Influence of Temperature on the Spatial Distribution of AuNPs on a Ceramic Substrate for Biosensing Applications. *Chemosensors* **2024**, *12*, 212. <https://doi.org/10.3390/chemosensors12100212>

Received: 25 July 2024

Revised: 7 October 2024

Accepted: 10 October 2024

Published: 15 October 2024



Copyright: © 2024 by the authors. Licensee MDPI, Basel, Switzerland. This article is an open access article distributed under the terms and conditions of the Creative Commons Attribution (CC BY) license (<https://creativecommons.org/licenses/by/4.0/>).

1. Introduction

Cancer, a leading cause of death worldwide, accounted for approximately 9.7 million deaths in 2022, with an estimated 20 million new cases reported globally each year [1]. Thus, the monitoring and early detection of diseases such as cancer are of great importance in improving patient outcomes and survival rates [2]. Early diagnosis significantly enhances treatment efficacy and survival rates, highlighting the critical need for advanced diagnostic

tools [3]. Traditional diagnostic methods, while effective, often involve invasive procedures that can be uncomfortable and risky for patients. Consequently, there is a growing demand for non-invasive sensors that can detect disease biomarkers with a high sensitivity and specificity. Non-invasive sensors offer numerous advantages, including reduced patient discomfort, lower risk of complication, and the ability to perform frequent monitoring [4].

Among the emerging technologies, surface-enhanced Raman spectroscopy (SERS) stands out for its potential to revolutionize disease diagnostics. SERS, a powerful technique in Raman spectroscopy, leverages the plasmonic properties of metallic nanoparticles to amplify Raman signals from molecules adsorbed on their surface [5]. This amplification allows for the detection of biomolecules at extremely low concentrations, making SERS an ideal candidate for non-invasive diagnostic applications. The recent advancements in plasmonic sensors, particularly those based on SERS, have opened new avenues in health monitoring [6]. These sensors typically utilize noble metal nanoparticles, such as gold nanoparticles (AuNPs), to enhance the Raman scattering of target molecules. The unique optical properties of AuNPs, including their strong surface plasmon resonance, make them highly effective in amplifying Raman signals [7,8]. This capability has led to the development of a new generation of SERS-based plasmonic sensors that can detect cancer biomarkers, pathogens, and other disease indicators with remarkable precision. In addition, gold nanoparticles have become a focal point in SERS research due to their excellent biocompatibility, stability, and tunable optical properties [9]. The controlled synthesis and functionalization of AuNPs are crucial for optimizing their performance in SERS applications. Research groups are particularly interested in understanding the growth mechanisms of AuNPs, as this knowledge is essential for developing reliable and reproducible SERS substrates [10]. The formation process of AuNPs significantly influences their size, shape, and surface properties, which in turn affect their plasmonic behavior and SERS performance. The development of SERS supports based on metallic nanoparticles supported on ceramic substrates is a promising trend in this field [5,11]. Ceramic materials, such as alumina (Al_2O_3), provide a stable and inert platform for anchoring AuNPs, enhancing their thermal and chemical stability. These hybrid substrates combine the advantageous properties of ceramics and noble metals, resulting in robust and efficient SERS platforms [12]. The integration of AuNPs with ceramic support has shown great potential in various applications, including environmental monitoring [13], food safety [14], and medical diagnostics [15]. Understanding the implications of the growing mechanism in the thermal-based fabrication of SERS substrates is vital for advancing this technology. The temperature at which AuNPs are synthesized can significantly impact their nucleation and growth processes, leading to variations in particle size, distribution, and morphology [16]. These parameters are critical in determining the plasmonic properties and SERS performance of the substrates. By comprehensively studying the thermal effects on AuNP growth, researchers can optimize fabrication protocols to achieve consistent and high-quality SERS substrates. Despite these promising advancements, several challenges remain in the implementation of SERS-based sensors. One of the primary hurdles is the reproducibility of AuNP formation processes. Variation in synthesis conditions can lead to significant differences in the optical properties and SERS activity of the nanoparticles [16–19]. Achieving uniform and reproducible AuNPs is essential for the widespread adoption of SERS technology in clinical and industrial settings. Additionally, the stability and robustness of SERS substrates under real-world conditions are critical factors that need to be addressed to ensure reliable performance over extended periods [20]. Recent literature highlights a growing interest in the development of SERS substrates, with various architectures being explored, such as heterostructures [21], nanoparticles on nanowire arrays [22], three-dimensional nanoporous structures [23], mesoscopic star-shaped particles [24], and nano-garland arrays [25]. All of the aforementioned SERS substrate architectures are gold-based, and the literature focuses on the following two main aspects: (1) increasing the Raman enhancement factor and (2) achieving a greater homogeneity in the Raman enhancement across the entire sample. Recent studies have proposed the use of Rhodamine-functionalized nanoparticles for identifying carcinogenic

cells and biomarkers [26–28]. Consequently, achieving the detection of Rhodamine via SERS substrates could pave the way for the development of biosensing technology [29].

In this work, the spatial distribution of AuNPs on a ceramic substrate was controlled by varying the length of time of thermal treatment on a gold film. The time was varied as a parameter to control the temperature propagation on the sample during thermal treatment. The SERS enhancements resulting from the different distributions of AuNPs on the ceramic were studied to explore the viability of employing the proposed material as a SERS substrate for breast cancer biomarkers.

2. Materials and Methods

2.1. Chemicals and Materials

For the development of this research, the following commercially available materials were obtained: sodium hydroxide (NaOH, SKU: 306576-100G), Rhodamine 6G (R6G, $C_{28}H_{31}N_2O_3Cl$, SKU: 56226-25MG), aluminum foil (Al, SKU: 326860-3.6G), oxalic acid ($C_2H_2O_4$, SKU: 247537-500G), perchloric acid ($HClO_4$, SKU: 311421-250ML), phosphoric acid (H_3PO_4 , SKU: 695017-500ML), and deionized water (H_2O , SKU: W4502-1L, 18 M Ω). All chemical reagents were commercially acquired from SIGMA-ALDRICH and used as received without any additional purification.

2.2. The Synthesis of AuNPs on the AAO Substrate

The AAO substrate was synthesized using the two-step anodization method [5]. Briefly, an aluminum sheet was cut into 1 cm \times 1 cm squares and mechanically polished to a mirror-like finish. The aluminum was then electrochemically polished in a solution of perchloric acid and ethanol mixed at a 4:1 volume ratio using a potentiostat under a constant voltage of 20 V (with respect to the reference electrode) for 1 min at room temperature. The samples were cleaned by subjecting them to alternating ultrasonic baths of deionized water and methanol for four cycles, each lasting 10 min. After cleaning, the samples were dried using a nitrogen stream. Next, the polished substrate underwent anodization to form alumina on the aluminum surface. This process was carried out using a potentiostat in a 3 M oxalic acid solution, applying a voltage of 20 V (with respect to the reference electrode) for 2 h at 4 $^{\circ}C$.

The initial alumina layer was removed by immersing the samples in a 0.5 M phosphoric acid solution for 20 min. A second anodization was then performed under the same conditions as the first, but extended over a period of 6 h. After completing this process, the samples were cleaned using six alternating ultrasonic baths of deionized water and methanol, each lasting 15 min, and were subsequently dried using a nitrogen stream. After obtaining the AAO substrate, a gold layer was deposited as a precursor for nanoparticle formation. The gold layer was deposited using sputtering coater equipment, employing an ionic current density of 16 mA/cm² and a vacuum of 5 Pa. Following gold deposition, an isothermal treatment was carried out in a horizontal furnace with a nitrogen flow (30 L/min) at 450 $^{\circ}C$. Four duration times were explored: (a) 5 min, (b) 15 min, (c) 30 min, and (d) 60 min. Based on the equipment calibration, the Au layer deposited had a thickness of 90 nm. Following deposition, the substrates underwent a cleaning process involving four ultrasonic bath cycles, alternating between methanol for 10 min and deionized water for 15 min. The samples were then dried using a nitrogen stream. Figure 1 summarizes the methodology followed to obtain the AuNPs on the AAO.

2.3. Physical Characterization of the Samples

The samples were characterized by field emission scanning electron microscopy (FE-SEM) using an AURIGA microscope equipped with a secondary electron (SE) detector (Zeiss, Jena, Germany). Images were acquired at an accelerating voltage of 2 keV and a working distance of 8 mm. For a detailed study of the gold nanostructures on the alumina substrate surface, images were obtained using scanning transmission electron microscopy (STEM) in a JEOL ARM200F (JEOL, Tokyo, Japan). Sixty images covering a total area of

10 $\mu\text{m} \times 10 \mu\text{m}$ were taken for each sample to obtain the statistical analysis for diameter size and interparticle distance. Prior to imaging, samples were prepared using a focused ion beam (FIB) system (JIB-4500 MultiBeam, JEOL, Tokyo, Japan) with a gallium liquid metal ion source (Ga). Atomic force microscopy (AFM) images were recorded with a microscope from SOL instruments (NT-MDT model) (NT-MDT spectrum instruments, Moscow, Russia). The samples were measured by AFM at 4 $^{\circ}\text{C}$ with an acquisition time of 10 min to record a 5 $\mu\text{m} \times 5 \mu\text{m}$ area for each sample. To obtain the particle size and interparticle distance, DigitalMicrograph software (version number 1.0) was used. A sample of 5000 particles were randomly analyzed through the acquisition of electron microscopy images. The measurements were then computed using image processing techniques included in the software, as has been conducted in other research work [19].

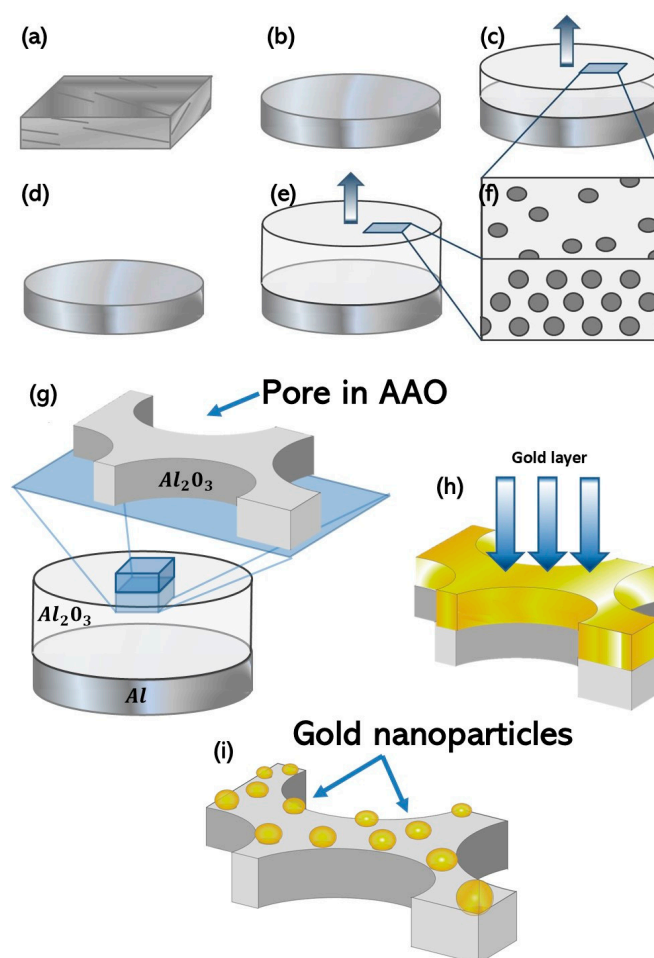


Figure 1. A schematic representation of AuNP dispersion on the alumina support after the (a) Al foil, (b) first electropolish, (c) alumina growth, (d) second electropolish, (e) second alumina growth, (f) pore comparison between the first and second anodization, (g) the alumina cleaning process, (h) gold layer deposition, and (i) final result of AuNPs on the AAO substrate.

2.4. Spatial Distribution Analysis for Biosensing Applications

The spatial distribution of AuNPs under the four different conditions was analyzed using Raman spectroscopy (LabRam HR800, Horiba Jovin Yvon spectrometer with a 633 nm excitation source) (Horiba, Kyoto, Japan). Rhodamine 6G (R6G) was used as the probe molecule due to its well-documented Raman response in SERS substrates [5]. In addition to analyzing the distribution of AuNPs, Raman mapping was performed on the substrate to assess the uniformity of signal enhancement across the proposed SERS substrate (AuNPs on AAO).

3. Results and Discussion

The anodized aluminum oxide (AAO) achieved was cylinder-like and porous, with a diameter of $102 \text{ nm} \pm 11 \text{ nm}$ and an average interpore distance of $145 \text{ nm} \pm 15 \text{ nm}$, as shown in the frontal view (Figure 2a) and lateral view (Figure 2b) of the AAO images recorded by FE-SEM. Once the AuNPs on the AAO substrate were obtained, top-view images were acquired using FE-SEM at the same magnification ($100,000\times$) to compare the distribution of nanoparticles on the alumina substrate (see Figure 3). At 450°C for 5 min, the resulting AuNPs exhibited a spherical shape with relatively homogeneous distribution across the AAO substrate (see Figure 3a). When the exposure time was increased to 15 min, the nanoparticles decreased in diameter and the distance between them also reduced (see Figure 3b). With a further increase in time to 30 min at 450°C , the AuNPs dramatically increased in their average diameter and the distance between them also increased (see Figure 3c). Finally, when the exposure time exceeded 60 min, the AuNPs lost their regular shape and formed larger gold particles, seemingly due to the accumulation of AuNPs (see Figure 3d). The distance between these larger gold particles increased, reflecting the loss of their nanoscale size. Note that the darker lines in Figure 3b are the result of charge effects within the scanning electron microscope, which is common in alumina-based sample analysis, as it is an electrical isolator material [30]. It is possible that AAO allows for the special dispersion of AAO due to the temperature propagation during thermal treatment and the surface energy relationship between the gold and the aluminum oxide.

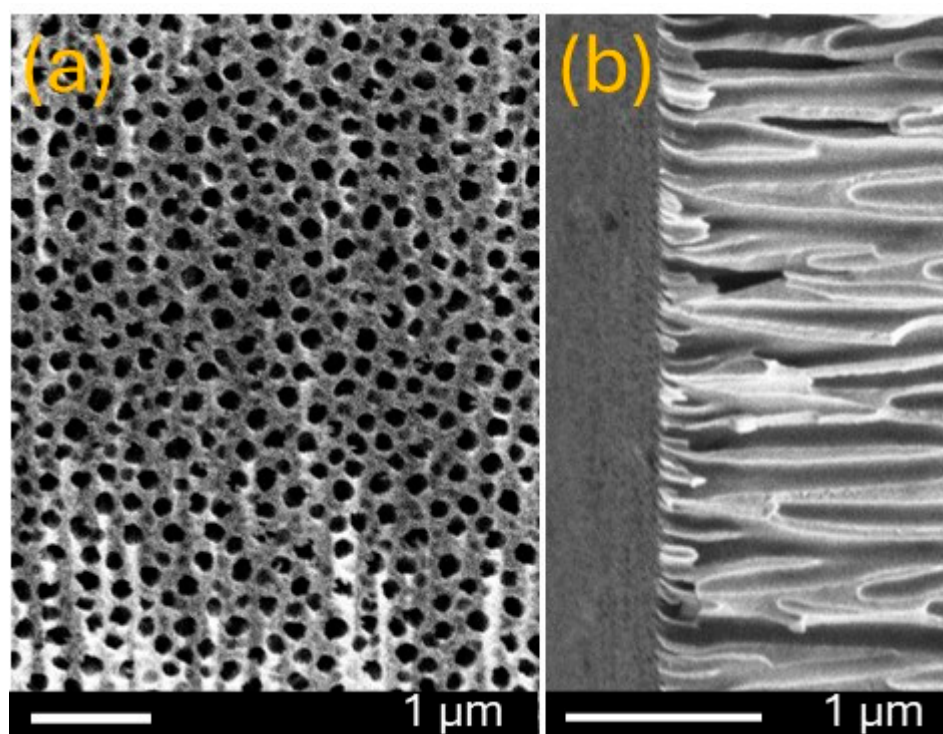


Figure 2. FE-SEM image of (a) frontal view and (b) lateral view of AAO substrate.

Combined with the FE-SEM analysis, a STEM analysis was conducted to study the spatial distribution of AuNPs on the alumina substrate. Figure 3a shows the AuNPs attached to the alumina pre-processed by FIB and obtained under a synthesis time of 15 min, where it can be seen that chemical bonding allows for the attachment of the AuNPs to the support [31]. A detailed image of the highlighted section in Figure 4a is shown in Figure 4b, where a clear difference in contrast indicates the phase difference between the nanoparticles and the substrate, attributed to gold and aluminum oxide, respectively [32,33]. Additionally, as metrics for the distribution of nanoparticles on the AAO substrate, two magnitudes were considered: (1) the diameter of the AuNPs, and (2) the

interparticle distance between the AuNPs. Thus, Figure 4c compares the average diameter size measured for each condition, showing values of $50 \text{ nm} \pm 5.9 \text{ nm}$, $27 \text{ nm} \pm 2.6 \text{ nm}$, $150 \text{ nm} \pm 60.1 \text{ nm}$, and $250 \text{ nm} \pm 80.6 \text{ nm}$ for the samples synthesized under conditions 1 (5 min), 2 (15 min), 3 (30 min), and 4 (60 min), respectively. On the other hand, the average interparticle distance was experimentally determined (see Figure 4d) to be $21 \text{ nm} \pm 2.3 \text{ nm}$, $9.0 \text{ nm} \pm 0.8 \text{ nm}$, $60.1 \text{ nm} \pm 6.4 \text{ nm}$, and $95.3 \text{ nm} \pm 11.2 \text{ nm}$ for synthesis conditions 1, 2, 3, and 4, respectively. These results suggest that temperature has a significant effect on the spatial distribution of AuNPs on a ceramic AAO substrate. A 15-min exposure promotes the smallest nanoparticle size diameter and the smallest interparticle distance, while a 60-min exposure results in the largest size for both the average diameter and the interparticle distance. This behavior can be explained according to classical nucleation theory and the growth phase in crystals, promoted by temperature, as reported in other systems [16,34].

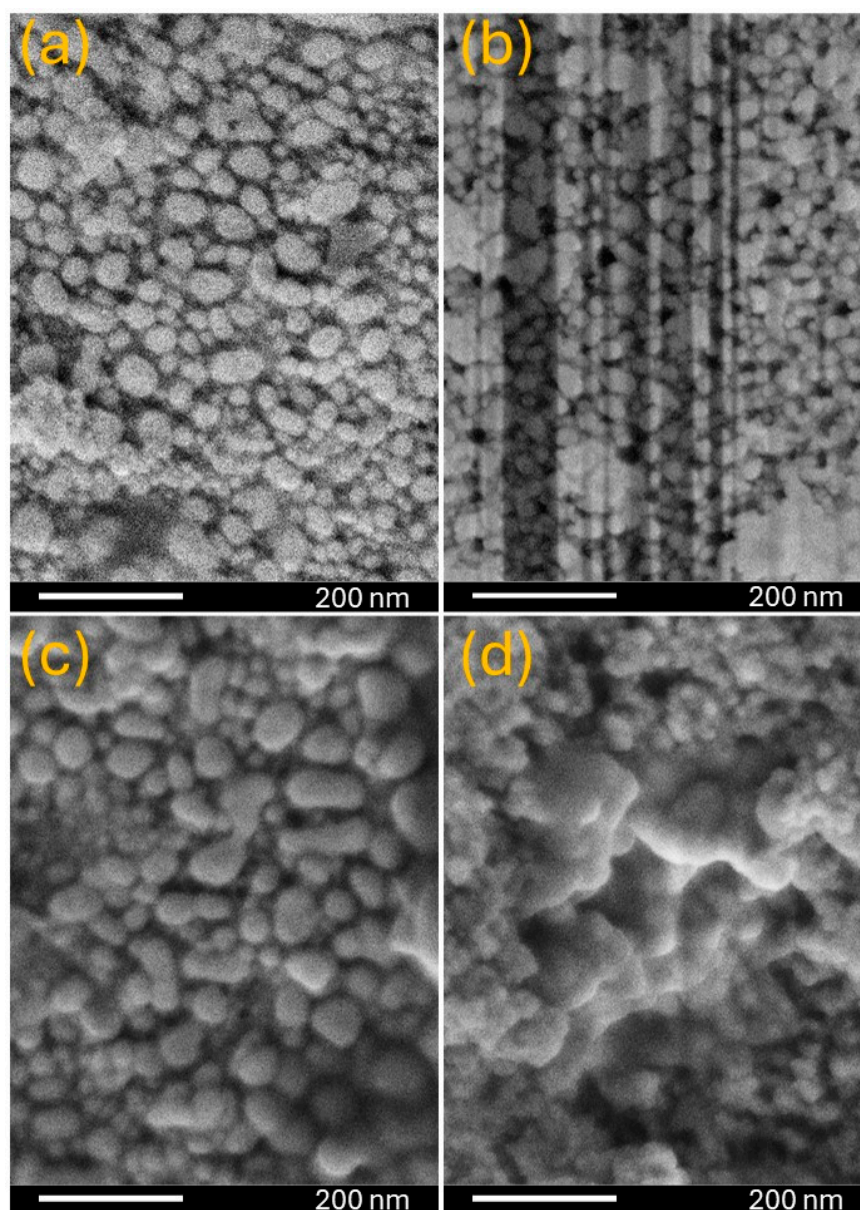


Figure 3. Field-emission scanning electron microscopy images from a top view of the AuNPs on the alumina, obtained by exposing the Au layer on the alumina to a temperature of 450°C for (a) 5 min, (b) 15 min, (c) 30 min, and (d) 60 min.

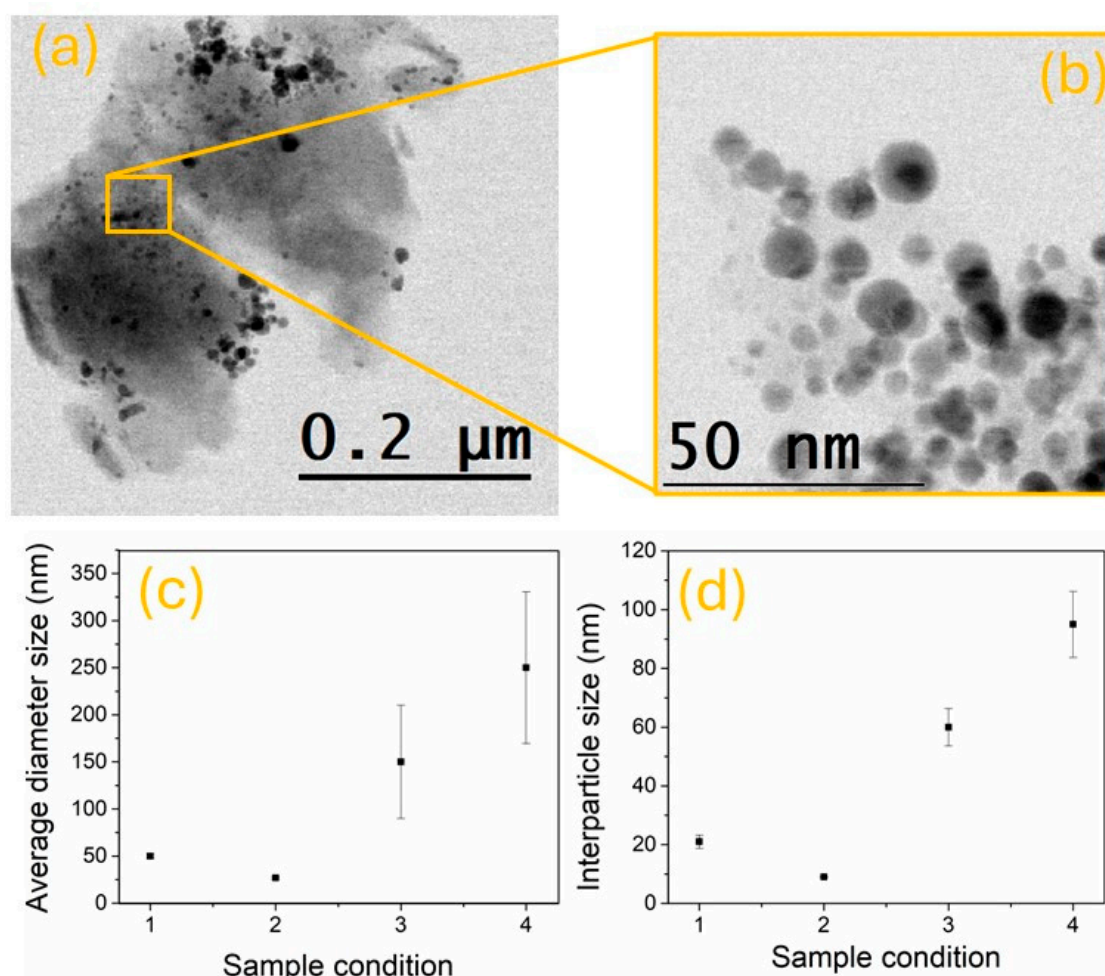


Figure 4. AuNPs on the AAO substrate, imaged using scanning transmission electron microscopy at a (a) low magnification and a (b) higher magnification. (c) Display of the average diameters of the AuNPs. (d) The average interparticle distance for each analyzed synthesis condition of AuNPs.

To determine the homogeneity offered by the substrates as potential sensors assisted by Raman spectroscopy, a 1×10^{-10} M Rhodamine 6G (R6G) solution was applied to interact with the synthesized substrates (AuNPs on alumina). A comparison of the lateral view of the interface between the alumina and AuNPs, imaged by recording backscattered electrons (BSE; Figure 5a), and secondary electrons (SE; Figure 5b), in the FE-SEM of samples incubated with the R6G solution, suggests that the spaces generated by the AuNPs and the porosity in the alumina play a key role in R6G adsorption on the surface (as depicted in the scheme shown in Figure 5c). This is supported by the fact that the AuNP accumulation appears thinner in the BSE image compared to the SE image, as organic materials do not provide sufficient signals in the BSE image due to their lower density and atomic number compared to the AuNPs [35,36]. Consequently, a SERS mapping was constructed from the R6G measured on all synthesized substrates. Raman spectroscopy was performed on the sample surface with 10 accumulative measurements and a recording time of 10 s each. The measurements were then repeated at 100 points on the sample to build a matrix of 100 pixels, where the intensity of the peak at 1361 cm^{-1} was used as the parameter to assign a color representing the magnitude. Figure 5e shows the resulting image of this adaptation, corresponding to the Raman mapping of the AuNPs on the AAO substrate, obtained at 450°C for 15 min. The R6G can be adsorbed by the AuNPs and the AAO, as shown in Figure 5a,b. Thus, the variation observed in Figure 5d,e could be influenced by the spatial distribution of AuNPs on the AAO.

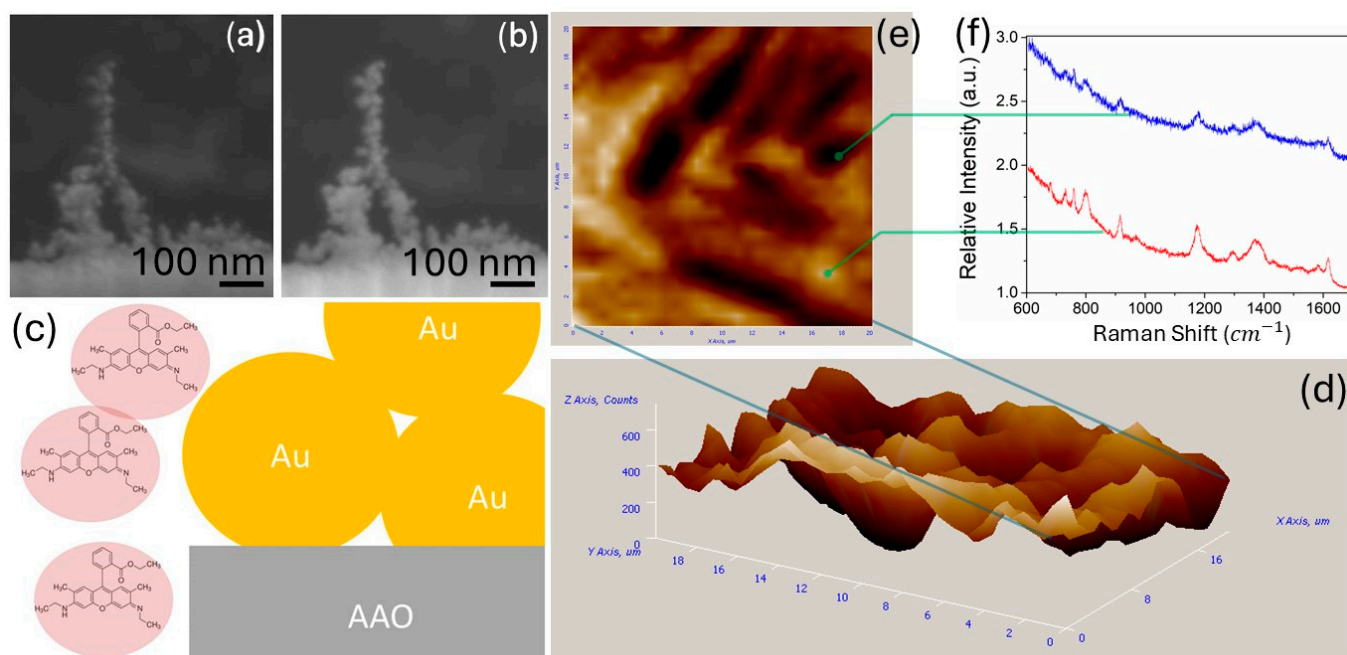


Figure 5. FE-SEM images of AuNPs on the alumina incubated with R6G, captured using (a) BSE and (b) SE detectors. (c) A schematic representation of the interactions between the substrate (AuNPs on AAO) and R6G. (d) A 3D projection of the Raman mapping, (e) a 2D projection of the Raman mapping, and a (f) Raman spectrum comparison between the highest intensity point and the lowest intensity point in the matrix of mapping.

Figure 5d shows a Raman mapping of AuNPs on an alumina support loaded with R6G; this image allows us to see the difference between the maximum intensity and the minimum intensity given by the SERS substrate developed in this work. Figure 5f compares the Raman spectra between the points with the highest and lowest intensities in the Raman mapping. The primary difference between these spectra is the noise level in the signal, while the peaks observed are consistent with those typically exhibited by R6G [5,37], as shown in Table 1. A common issue with substrates used in SERS-based sensors is the homogeneity of the enhancement effect over a large area of the sample. To evaluate the improvement in homogeneity of the Raman scattering, a large Raman mapping ($5\ \mu\text{m} \times 5\ \mu\text{m}$ area) was conducted on the synthesized samples with R6G in five sections of the substrate, with each section separated by at least 4 mm. In addition, the enhancement factor was computed for each sample. Thus, the known methodology for computing the EF was employed [5]. The minimum concentration detected for each sample was employed to compute the EF, 1×10^{-10} M, 1×10^{-9} M, 1×10^{-7} M, and 1×10^{-6} M, in the samples treated for 5 min, 15 min, 30 min, and 60 min, respectively. A $1\ \mu\text{L}$ drop was applied to the AAO/AuNPs and allowed to dry prior to measurement. To assess the intensity from the R6G alone, 1×10^{-11} g of R6G was analyzed in its solid state. Based on the probe diameter ($10\ \mu\text{m}$), the estimated number of irradiated R6G molecules was 1.257×10^{11} in the lyophilized sample, 1.3257×10^5 for the 1×10^{-10} M, 1.1134×10^6 in the 1×10^{-9} M, dilution, 2.5344×10^7 for the 1×10^{-8} M, 3.4615×10^8 for the 1×10^{-7} M, and 2.6522×10^9 in the 1×10^{-6} M dilution. Raman spectra were subsequently recorded for all samples. The peak intensity corresponding to the vibrational mode at $1184\ \text{cm}^{-1}$ was evaluated, yielding intensity values. The solid R6G sample recorded an intensity value of 184.35. Then, the relationship between Raman intensity due to the SERS effect and the R6G sole was computed to determine the EF. The computation was repeated randomly at ten different points on the sample, recording both the minimum and maximum Raman intensity values for each sample, resulting in a range of minimum and maximum values of

0.1×10^5 – 0.5×10^5 , 0.9×10^6 – 1.1×10^6 , 5.2×10^4 – 6.8×10^4 , and 2.3×10^2 – 4.5×10^3 for the samples, synthesized at 5 min, 15 min, 30 min, and 60 min, respectively.

Table 1. Vibrational moods attributed to Rhodamine 6G (in Figure 5f).

Peak Position in Figure 5f	Vibrational Mode
769 cm^{-1}	C–H out-of-plane bending
1184 cm^{-1}	C–H in-of-plane bending
1311 cm^{-1}	C–O–C stretching in COOC_2H_5 group
1358 cm^{-1}	C–C stretching in xanthene ring
1574 cm^{-1}	C–C stretching in phenyl ring
1645 cm^{-1}	C–C stretching in xanthene ring

Figure 6 shows two images obtained by AFM which show a 5 micrometer by 5 micrometer area of the AuNPs on the alumina substrate, particularly those synthesized at 15 min of thermal treatment. The topological features of the AuNPs on a single alumina substrate are displayed in Figure 6a, where the AuNPs on the alumina are distinguishable. The size of AuNPs is in good agreement with the FE-SEM and STEM results. After incubating the sample with the R6G solution for 60 min, the roughness of the sample decreases from 0.16 to 0.08, as seen in Figure 6b. Note that the mentioned difference can be better appreciated by comparing the roughness profile of the selected area shown in the inserts of Figure 6a,b. Note that sample becomes less rough because the R6G gets trapped on the surface. By comparing the Raman mapping with the topological characteristics of the sample, both before and after R6G incubation, the intensity variation of each point constructing the image exhibits only a slight average change compared to Figure 6a,b. This could be attributed to the R6G solution concentration, which was 1×10^{-10} M, the electrostatic forces in the sample that promote the physisorption of R6G, and the solvent used in the solution (deionized water).

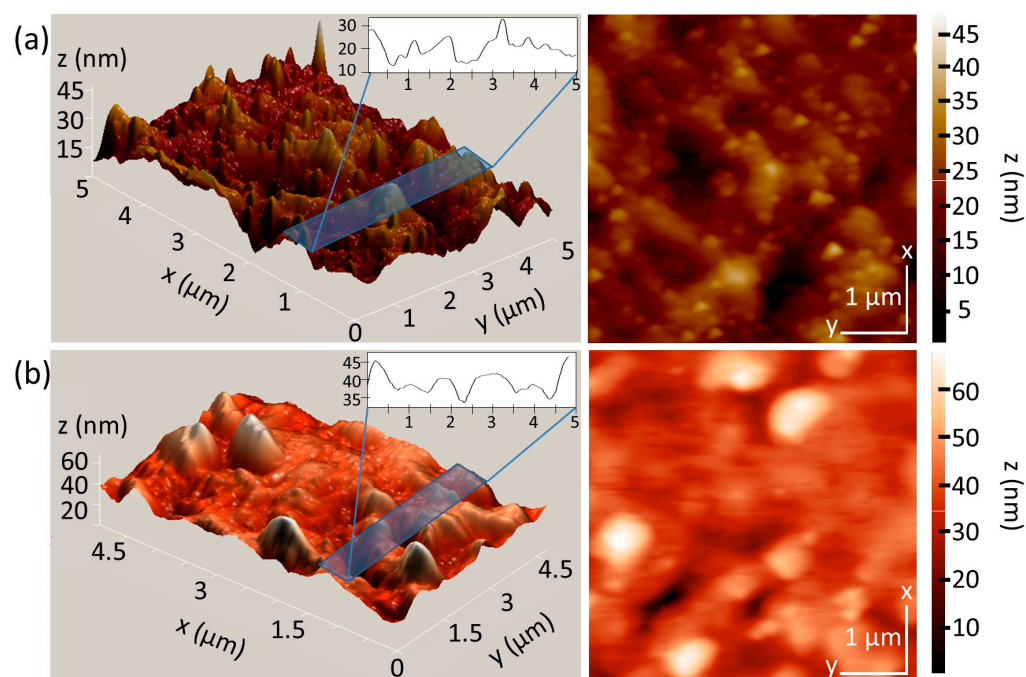


Figure 6. The AFM image of AuNPs on an alumina substrate (a) before and (b) after incubation with the R6G solution. Each set of images displays a 3D projection (left) and a 2D projection (right).

On the other hand, the recorded Raman mapping of the same sample exhibited in Figure 6b is shown in Figure 7. Note that images shown in Figures 6 and 7 correspond to the same area in the sample. It can be observed that the roughness profile shown (insets in Figure 7) indicate that the sample has a homogeneous SERS effect across the entire area. The maximum intensity deviation (D) is a parameter that provides information on the reproducibility of the SERS effect in active SERS substrates. For the samples, this parameter was calculated using Equation (1), where the difference between the maximum peak intensity and the average peak intensity (ΔI) of a certain number of samples is divided by the average peak intensity (\bar{I}) and multiplied by 100 to obtain the percentage value of D .

$$D = \frac{\Delta I}{\bar{I}} \cdot 100\% \quad (1)$$

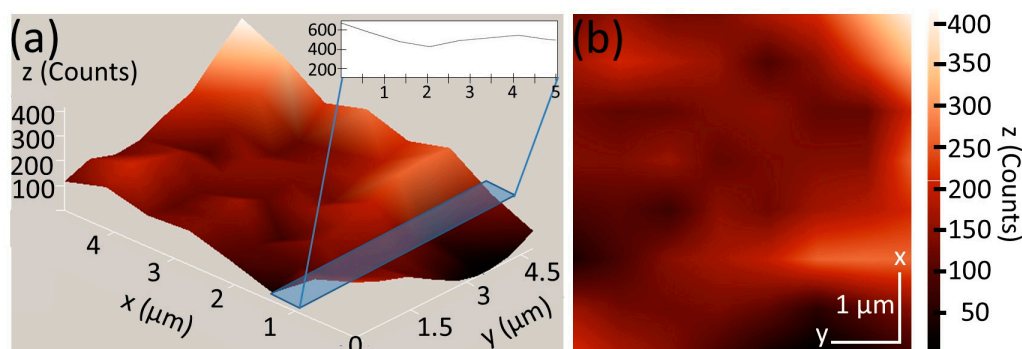


Figure 7. (a) Raman mapping of the sample shown in (b). Each set of images displays a 3D projection (left) and a 2D projection (right).

The intensity of fifteen points at different places on the same sample were measured to calculate the statistics (Table 2). According to M. J. Natan [38], the values of maximum intensity deviation should be below 20%. Based on the calculated values, all samples meet these criteria, indicating that even though all the samples are suitable for application as SERS substrates, the sample synthesized in condition 2 is the best candidate for this application.

Table 2. A comparison between the characteristic values for computing the maximum intensity deviation of the synthesized substrates.

Sample	\bar{I}	ΔI	D (%)
1	140.18	24.59	17.54
2	408.2	74.96	18.36
3	191.46	30.39	15.87
4	57.88	11.31	19.54

To evaluate the influence of a ceramic substrate on the performance of SERS substrates for biosensing applications, the process of SERS substrate formation was repeated using a (111) silicon wafer as a reference. Figure 8 presents FE-SEM images of samples treated for 5, 15, 30, and 60 min. It is evident that the formation of AuNPs is not homogeneous under any condition, with a broad size distribution observed in all cases. This indicates that the ceramic substrate plays a crucial role in the spatial distribution of AuNPs, particularly during the thermal treatment process. These findings suggest that ceramic substrates significantly enhance the homogeneity of SERS substrates over large areas, which is essential for obtaining reliable Raman spectroscopy measurements in biosensing applications.

The novelty of this work addresses one of the main challenges in applying SERS substrates to biosensing technology: achieving homogeneity in the SERS effect across the entire substrate. Compared to other studies, the proposed substrate offers a significant

contribution by achieving large-area substrates with high reproducibility in SERS amplification and acceptable homogeneity [39–41]. Despite these advancements, SERS substrates must combine homogeneity, accessibility, and enhancement to be commercially viable in the medical sector.

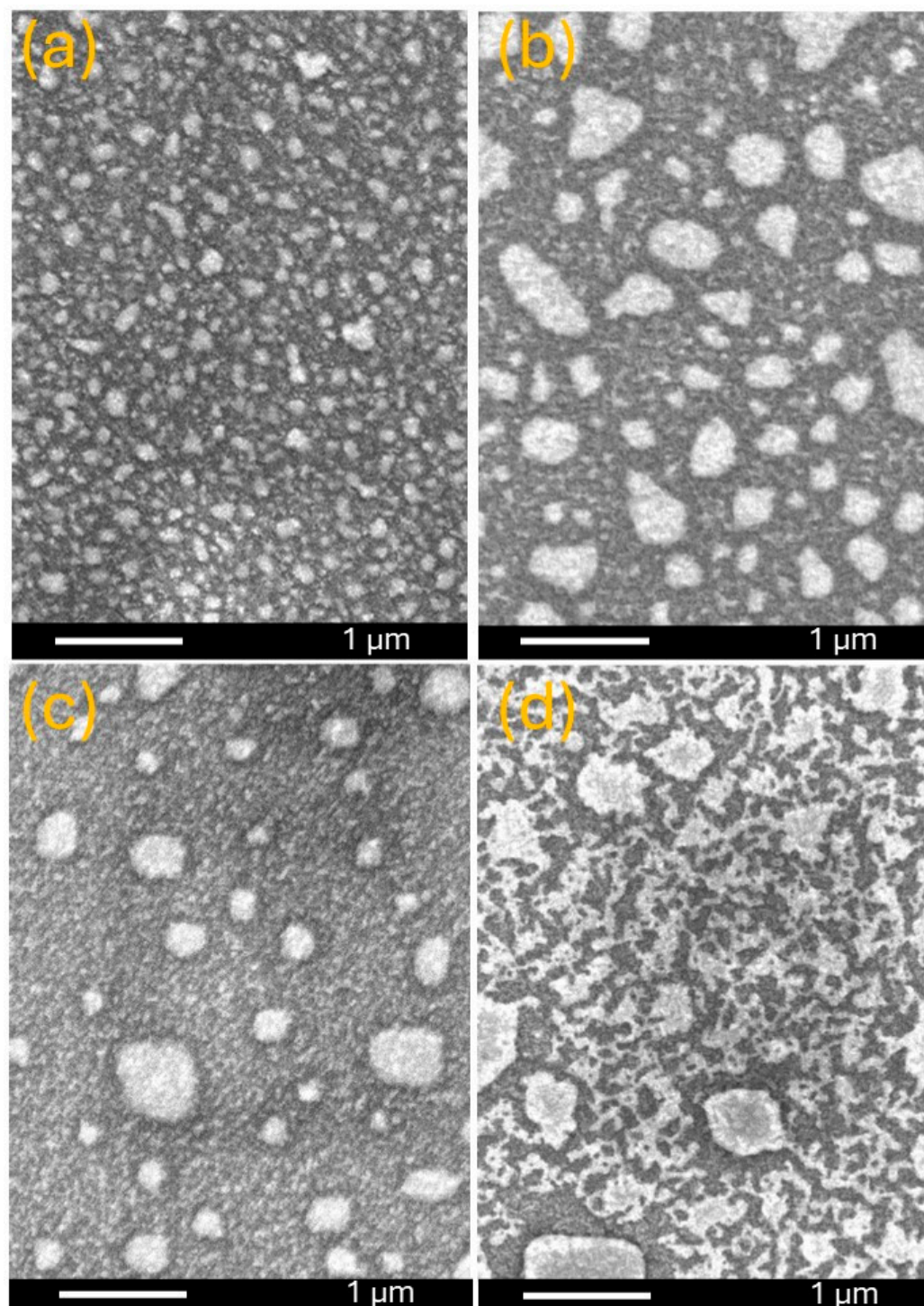


Figure 8. Field-emission scanning electron microscopy images from a top view of AuNPs on silicon wafer, obtained by exposing the Au layer on the alumina to a temperature of 450 °C for (a) 5 min, (b) 15 min, (c) 30 min, and (d) 60 min.

4. Conclusions

This study successfully demonstrates the potential of gold nanoparticles (AuNPs) on alumina (AAO) substrates as effective surface-enhanced Raman scattering (SERS) biosensors due to an increase in the SERS effect's homogeneity by thermal treatment. Through meticulous control of thermal treatment duration, we were able to significantly influence the spatial distribution and size of AuNPs, where shorter treatments (15 min at 450 °C) yielded smaller and more closely spaced nanoparticles and longer treatments resulted in larger and more dispersed particles. The combined analyses using field-emission scanning electron microscopy (FE-SEM), scanning transmission electron microscopy (STEM), and atomic force microscopy (AFM) confirmed the morphology and topological features of the AuNPs on the alumina substrate. AAO can influence the propagation of temperature and allow for a high special dispersion of AuNPs. The Raman mapping, conducted with Rhodamine 6G (R6G) as a probe molecule, revealed a homogeneous SERS enhancement across the substrate, with the sample synthesized for 15 min exhibiting the most favorable characteristics. This condition provided the smallest average nanoparticle size and interparticle distance, contributing to a more uniform and reproducible SERS signal. The reproducibility of the SERS effect was further validated by the maximum intensity deviation (D), which remained below 20% in all samples, confirming their reliability for sensor applications. These findings underscore the significance of having precise control over synthesis parameters when optimizing the performance of SERS substrates. The optimized AuNPs on the alumina substrate synthesized under conditions of 15 min at 450 °C show great promise as SERS-based sensors. These optimized features were achieved due to temperature distribution during the thermal treatment and were controlled by the duration time of the process.

Author Contributions: Conceptualization, Y.M.H.-R.; methodology, Y.M.H.-R. and E.B.-L.; software, Y.M.H.-R. and E.B.-L.; validation, P.D.-M., C.H.G.d.I.R. and O.E.C.-M.; formal analysis, Y.M.H.-R. and E.B.-L.; investigation, Y.M.H.-R. and E.B.-L.; resources, C.H.G.d.I.R. and O.E.C.-M.; data curation, P.D.-M., C.H.G.d.I.R. and O.E.C.-M.; writing—original draft preparation, Y.M.H.-R. and E.B.-L.; writing—review and editing, P.D.-M., C.H.G.d.I.R. and O.E.C.-M.; visualization, Y.M.H.-R., E.B.-L. and P.D.-M.; supervision, C.H.G.d.I.R. and O.E.C.-M.; project administration, C.H.G.d.I.R. and O.E.C.-M.; funding acquisition, C.H.G.d.I.R. and O.E.C.-M. All authors have read and agreed to the published version of the manuscript.

Funding: This research was funded by the Secretaría de Investigación y Posgrado del Instituto Politécnico Nacional (SIP-IPN), the Universidad Autónoma Metropolitana (UAM), and the Secretaría de Educación, Ciencia, Tecnología e Innovación (SECTEI), grant number SIP-2024-RE/034.

Institutional Review Board Statement: Not applicable.

Informed Consent Statement: Not applicable.

Data Availability Statement: All data contained in this work is available on request to the corresponding author.

Acknowledgments: The authors would like to express their gratitude to Secretaría de Investigación y Posgrado of the Instituto Politécnico Nacional (SIP-IPN), Universidad Autónoma Metropolitana (UAM), and Secretaría de Educación, Ciencia, Tecnología e Innovación (SECTEI) for their financial support of this research. This study was conducted at the Laboratorio de Sistemas para Diagnóstico y Tratamiento de Cáncer at UPIITA-IPN.

Conflicts of Interest: The authors declare no conflicts of interest. The funders had no role in the design of the study; in the collection, analyses, or interpretation of data; in the writing of the manuscript; or in the decision to publish the results.

References

- World Health Organization. Global Cancer Burden Growing, Amidst Mounting Need for Services, International Agency for Research on Cancer. 2024. Available online: <https://www.who.int/> (accessed on 3 October 2024).
- Zhou, Y.; Tao, L.; Qiu, J.; Xu, J.; Yang, X.; Zhang, Y.; Tian, X.; Guan, X.; Cen, X.; Zhao, Y. Tumor biomarkers for diagnosis, prognosis and targeted therapy. *Signal Transduct. Target. Ther.* **2024**, *9*, 132. [\[CrossRef\]](#) [\[PubMed\]](#)
- Kuklinski, D.; Blum, M.; Subelack, J.; Geissler, A.; Eichenberger, A.; Morant, R. Breast cancer patients enrolled in the Swiss mammography screening program “donna” demonstrate prolonged survival. *Breast Cancer Res.* **2024**, *26*, 84. [\[CrossRef\]](#)
- Keerthana, S.; Saquib, M.; Poojary, H.; Illanad, G.; Valavan, D.; Selvakumar, M.; Nayak, R.; Mazumder, N.; Ghosh, C. Skin emitted volatiles analysis for noninvasive diagnosis: The current advances in sample preparation techniques for biomedical application. *RSC Adv.* **2024**, *14*, 12009–12020. [\[CrossRef\]](#)
- Cigarroa-Mayorga, O.; Gallardo-Hernández, S.; Talamás-Rohana, P. Tunable Raman scattering enhancement due to self-assembled Au nanoparticles layer on porous AAO: The influence of the alumina support. *Appl. Surf. Sci.* **2021**, *536*, 147674. [\[CrossRef\]](#)
- Li, D.; Yue, W.; He, Q.; Gao, P.; Gong, T.; Luo, Y.; Wang, C.; Luo, X. Single-molecule detection of SARS-CoV-2 N protein on multilayered plasmonic nanotraps with surface-enhanced Raman spectroscopy. *Talanta* **2024**, *278*, 126494. [\[CrossRef\]](#) [\[PubMed\]](#)
- Wang, K.-S.; Lin, H.-T.; Wen, Y.-J.; Huang, L.-Y.; Yang, M.-C.; Liu, T.-Y. Thiol-functionalized mesoporous silica-embedded AuNPs with highly sensitive substrates for surface-enhanced Raman scattering detection. *Surf. Coat. Technol.* **2024**, *483*, 130814. [\[CrossRef\]](#)
- Sun, M.; Xie, M.; Jiang, J.; Qi, Z.; Wang, L.; Chao, J. Customized Self-Assembled Gold Nanoparticle-DNA Origami Composite Templates for Shape-Directed Growth of Plasmonic Structures. *Nano Lett.* **2024**, *24*, 6480–6487. [\[CrossRef\]](#)
- Borah, D.; Mishra, V.; Debnath, R.; Ghosh, K.; Gogoi, D.; Rout, J.; Pandey, P.; Ghosh, N.N.; Bhattacharjee, C.R. Facile green synthesis of highly stable, water dispersible carbohydrate conjugated Ag, Au and Ag-Au biocompatible nanoparticles: Catalytic and antimicrobial activity. *Mater. Today Commun.* **2023**, *37*, 107096. [\[CrossRef\]](#)
- Das, A.; Pant, U.; Cao, C.; Moirangthem, R.S.; Kamble, H.B. Wearable Surface-Enhanced Raman Spectroscopy Sensor Using Inverted Bimetallic Nanopyramids for Biosensing and Sweat Monitoring. *ACS Appl. Opt. Mater.* **2023**, *1*, 1938–1951. [\[CrossRef\]](#)
- Wang, X.; Chen, C.; Zuo, E.; Han, S.; Yang, J.; Yan, Z.; Lv, X.; Hou, J.; Jia, Z. Novel SERS biosensor for rapid detection of breast cancer based on Ag₂O-Ag-PSi nanochips. *Spectrochim. Acta Part A Mol. Biomol. Spectrosc.* **2023**, *303*, 123226. [\[CrossRef\]](#)
- Guselnikova, O.; Trelin, A.; Kang, Y.; Postnikov, P.; Kobashi, M.; Suzuki, A.; Shrestha, L.K.; Henzie, J.; Yamauchi, Y. Pretreatment-free SERS sensing of microplastics using a self-attention-based neural network on hierarchically porous Ag foams. *Nat. Commun.* **2024**, *15*, 4351. [\[CrossRef\]](#) [\[PubMed\]](#)
- Sharipov, M.; Kakhkhorov, S.A.; Tawfik, S.M.; Azizov, S.; Liu, H.-G.; Shin, J.H.; Lee, Y.-I. Highly sensitive plasmonic paper substrate fabricated via amphiphilic polymer self-assembly in microdroplet for detection of emerging pharmaceutical pollutants. *Nano Converg.* **2024**, *11*, 13. [\[CrossRef\]](#) [\[PubMed\]](#)
- Li, H.; Sheng, W.; Hassan, M.; Geng, W.; Chen, Q. Quantification of antibiotics in food by octahedral gold-silver nanocages-based SERS sensor coupling multivariate calibration. *Spectrochim. Acta Part A Mol. Biomol. Spectrosc.* **2024**, *320*, 124595. [\[CrossRef\]](#) [\[PubMed\]](#)
- Sahafnejad, Z.; Hashemzadeh, H.; Allahverdi, A.; Fathi, A.; Saievar-Iranizad, E.; Naderi-Manesh, H. Sensitive detection of miR-9 in human serum: An electrochemical approach utilizing robust gold nanostructures for early diagnosis of lung cancer. *Talanta Open* **2023**, *8*, 100272. [\[CrossRef\]](#)
- Mendoza-Sánchez, A.R.; Hernández-Rodríguez, Y.; Casas-Espínola, J.; Cigarroa-Mayorga, O. Nanostructural modulation of Schottky barrier in Au/ α -MoO₃ heterojunction via Au nanoparticle size control. *Appl. Surf. Sci.* **2024**, *670*, 160624. [\[CrossRef\]](#)
- Horta-Piñeres, S.; Cortez-Valadez, M.; Avila, D.A.; Leal-Perez, J.E.; Leyva-Porras, C.C.; Flores-Acosta, M.; Torres, C.O. Influence of Carboxymethyl Cellulose on the Green Synthesis of Gold Nanoparticles Using *Gliricidia sepium* and *Petiveria alliacea* Extracts: Surface-Enhanced Raman Scattering Effect Evaluation. *ACS Omega* **2023**, *8*, 46466–46474. [\[CrossRef\]](#)
- Zhou, H.; Shi, T.; Cai, W.; Wu, D. Rational design of Au NPs satellite nanostructure modified microelectrode for dual-mode detection of mercury ions in algal solution. *Electrochim. Acta* **2023**, *472*, 143461. [\[CrossRef\]](#)
- Saldivar-Ayala, D.; Ashok, A.; Cigarroa-Mayorga, O.; Hernández-Rodríguez, Y. Tuning the plasmon resonance of Au-Ag core-shell nanoparticles: The influence on the visible light emission for inorganic fluorophores application. *Colloids Surfaces A Physicochem. Eng. Asp.* **2023**, *677 Pt A*, 132359. [\[CrossRef\]](#)
- Liu, C.; Weber, S.; Peng, R.; Wu, L.; Zhang, W.-S.; Lippa, P.B.; Popp, J.; Cialla-May, D. Toward SERS-based therapeutic drug monitoring in clinical settings: Recent developments and trends. *TrAC Trends Anal. Chem.* **2023**, *164*, 117094. [\[CrossRef\]](#)
- Fang, T.; Wei, Q.; Wu, E.; Pu, H. Elevating electron transfer of recyclable SERS sensor using AuNPs/TiO₂/Ti₃C₂ heterostructures for detection of malachite green in sunfish. *Spectrochim. Acta Part A Mol. Biomol. Spectrosc.* **2025**, *325*, 125047. [\[CrossRef\]](#)
- Xu, D.; Zhou, L.; Zhang, S.; Wang, Z.; Yang, W.; Guo, Q.; Wang, Z.; Chen, J. Facile fabrication of Au-Ag alloy nanoparticles/Ag nanowires SERS substrates with bimetallic synergistic effect for ultra-sensitive detection of crystal violet and alkali blue 6B. *Spectrochim. Acta Part A Mol. Biomol. Spectrosc.* **2025**, *324*, 124981. [\[CrossRef\]](#) [\[PubMed\]](#)
- Zhang, Y.; Wang, H.; Ni, C.; Wang, Q.; Lin, T. Three-dimensional nanoporous gold/gold nanoparticles substrate for surface-enhanced Raman scattering detection of illegal additives in food. *Spectrochim. Acta Part A Mol. Biomol. Spectrosc.* **2024**, *323*, 124879. [\[CrossRef\]](#) [\[PubMed\]](#)

24. Kim, S.; Yoo, S.; Nam, D.H.; Kim, H.; Hafner, J.H.; Lee, S. Monodispersed mesoscopic star-shaped gold particles via silver-ion-assisted multi-directional growth for highly sensitive SERS-active substrates. *Nano Converg.* **2024**, *11*, 26. [[CrossRef](#)] [[PubMed](#)]
25. Fu, Y.-F.; Zhu, J.; Li, X.; Weng, G.-J.; Li, J.-J.; Zhao, J.-W. Au-Ag nano-garlands as a versatile SERS substrate: Two-step synthesis realizes the growth of petal-shaped branches on hollow Au-Ag nanoshells. *Colloids Surfaces A Physicochem. Eng. Asp.* **2024**, *698*, 134541. [[CrossRef](#)]
26. Liu, X.; Wang, Q.; Diao, Z.; Huo, D.; Hou, C. Label-free fluorescent biosensor based on AuNPs etching releasing signal for miRNA-155 detection. *Talanta* **2024**, *278*, 126481. [[CrossRef](#)]
27. Pallavi, P.; Harini, K.; Crowder, S.; Ghosh, D.; Gowtham, P.; Girigoswami, K.; Girigoswami, A. Rhodamine-Conjugated Anti-Stokes Gold Nanoparticles with Higher ROS Quantum Yield as Theranostic Probe to Arrest Cancer and MDR Bacteria. *Appl. Biochem. Biotechnol.* **2023**, *195*, 6979–6993. [[CrossRef](#)]
28. He, Q.; Liu, J.; Liang, J.; Liu, X.; Tuo, D.; Li, W. Chemically Surface Tunable Solubility Parameter for Controllable Drug Delivery—An Example and Perspective from Hollow PAA-Coated Magnetite Nanoparticles with R6G Model Drug. *Materials* **2018**, *11*, 247. [[CrossRef](#)]
29. Swanson, W.B.; Durdan, M.; Eberle, M.; Woodbury, S.M.; Mauser, A.; Gregory, J.; Zhang, B.; Niemann, D.; Herremans, J.; Ma, P.X.; et al. A library of Rhodamine6G-based pH-sensitive fluorescent probes with versatile in vivo and in vitro applications. *RSC Chem. Biol.* **2022**, *3*, 748–764. [[CrossRef](#)]
30. Cortés-Valadez, P.J.; Baños-López, E.; Hernández-Rodríguez, Y.M.; Cigarroa-Mayorga, O.E. Bryophyte-Bioinspired Nanoporous AAO/C/MgO Composite for Enhanced CO₂ Capture: The Role of MgO. *Nanomaterials* **2024**, *14*, 658. [[CrossRef](#)]
31. Wang, H.; Cai, J.; Wang, T.; Yan, R.; Shen, M.; Zhang, J.; Yue, X.; Wang, L.; Yuan, X.; Lv, E.; et al. Functionalized gold nanoparticle enhanced nanorod hyperbolic metamaterial biosensor for highly sensitive detection of carcinoembryonic antigen. *Biosens. Bioelectron.* **2024**, *257*, 116295. [[CrossRef](#)]
32. Abou-Ras, D.; Caballero, R.; Fischer, C.-H.; Kaufmann, C.; Lauermann, I.; Mainz, R.; Mönig, H.; Schöpke, A.; Stephan, C.; Streeck, C.; et al. Comprehensive Comparison of Various Techniques for the Analysis of Elemental Distributions in Thin Films. *Microsc. Microanal.* **2011**, *17*, 728–751. [[CrossRef](#)] [[PubMed](#)]
33. Tao, X.; Eades, A. Measurement and Mapping of Small Changes of Crystal Orientation by Electron Backscattering Diffraction. *Microsc. Microanal.* **2005**, *11*, 341–353. [[CrossRef](#)] [[PubMed](#)]
34. Mendoza-Sánchez, A.; Cano, F.J.; Hernández-Rodríguez, M.; Cigarroa-Mayorga, O. Influence of ZnO Morphology on the Functionalization Efficiency of Nanostructured Arrays with Hemoglobin for CO₂ Capture. *Crystals* **2022**, *12*, 1086. [[CrossRef](#)]
35. Mandal, S.; Singh, R.; Roy, D.; Mukhopadhyay, K.; Dwivedi, M.; Joshi, M. Insights into the hierarchical geometries of hybrid low-dimensional carbons. *Discov. Mater.* **2024**, *4*, 21. [[CrossRef](#)]
36. Kheradmandfard, M.; Kharazi, A.Z.; Javanmard, S.H.; Minouei, H.; Rahimzadeh, R.; Kim, D.-E. Architecting ultra-thin SiO₂ shell for high magnetic performance of Fe₃O₄ nanoparticles for biomedical applications. *Inorg. Chem. Commun.* **2024**, *168*, 112845. [[CrossRef](#)]
37. Zhang, Y.; Xu, Z.; Zhang, K.; Song, Y.; Dong, B.; Wang, J.; Yan, M.; Sun, Q. Fabrication of Superhydrophobic–Hydrophilic Patterned Cu@Ag Composite SERS Substrate via Femtosecond Laser. *Nanomanufacturing Metrol.* **2024**, *7*, 1. [[CrossRef](#)]
38. Natan, M.J. Concluding Remarks: Surface enhanced Raman scattering. *Faraday Discuss.* **2006**, *132*, 321–328. [[CrossRef](#)]
39. Sloan-Dennison, S.; Wallace, G.Q.; Hassanain, W.A.; Laing, S.; Faulds, K.; Graham, D. Advancing SERS as a quantitative technique: Challenges, considerations, and correlative approaches to aid validation. *Nano Converg.* **2024**, *11*, 33. [[CrossRef](#)]
40. Sibug-Torres, S.M.; Grys, D.-B.; Kang, G.; Niihori, M.; Wyatt, E.; Spiesshofer, N.; Ruane, A.; de Nijs, B.; Baumberg, J.J. In situ electrochemical regeneration of nanogap hotspots for continuously reusable ultrathin SERS sensors. *Nat. Commun.* **2024**, *15*, 2022. [[CrossRef](#)]
41. Lei, H.; Zhao, W.; Huang, F.; Tian, Y.; Zhao, Q.; Ma, R.; Ren, L.; Li, H.; Dou, S.; Wang, Z. Shell thickness-dependent Au@Ag nanoparticles for surface-enhanced Raman scattering detection of pollutants. *Vacuum* **2024**, *229*, 113577. [[CrossRef](#)]

Disclaimer/Publisher’s Note: The statements, opinions and data contained in all publications are solely those of the individual author(s) and contributor(s) and not of MDPI and/or the editor(s). MDPI and/or the editor(s) disclaim responsibility for any injury to people or property resulting from any ideas, methods, instructions or products referred to in the content.